ORIGINAL PAPER

Umberto Casellato · Nicola Comisso · Giovanni Davolio
Giuliano Mengoli

Charge storage in 40/60 TiFe alloy electrodes

Abstract Charge storage in 40/60 TiFe alloy has been investigated using electrode fabrication powder material, either of true alloy or of alloy precursor grades. The true alloy activated very reluctantly in that its maximum charge (i.e., hydrogen) capacity remained below 100 mA h g^{-1}. In contrast, the alloy precursor could be activated to an intrinsic capacity of $\sim$300 mA h g^{-1}. Charge storage of the 40/60 TiFe alloy precursor was certainly affected by the redox reactions of surface Fe, but a large amount was stored as hydrogen absorbed by the material, as indicated by a dialometric test and the poison effect. X-ray and EDAX analyses of the two materials can account for their differing abilities to store charge.

Keywords Hydrogen · Hydrides · Intermetallic compounds · Titanium-iron alloy · Electrolysis

Introduction

The surface of the air-exposed, crushed 50/50 TiFe intermetallic compound (IMC), which is the usual form of the commercial product, is covered by a 10–30 nm thick oxide layer impervious to hydrogen, and hence hydriding of the virgin IMC requires previous activation by pressurized hydrogen at temperatures between 300 and 400 °C [1]. The surface of the activated TiFe thus shows the presence of metallic Fe [1], which predictably serves as the gating force for dissociative hydrogen absorption.

U. Casellato
CNR ICTIMA, Istituto di Chimica,
Corso Stati Uniti 4, 35127 Padua, Italy

N. Comisso · G. Mengoli (✉)
CNR IPELP, Istituto di Polarografia,
Corso Stati Uniti 4, 35127 Padua, Italy
E-mail: gmengoli@ipelp.pd.cnr.it
Fax: +39-049-829-5853

G. Davolio
Università di Modena, Dipartimento di Chimica,
Via Campi 183, 41100 Modena, Italy

We recently found [2] that polycrystalline 50/50 TiFe can (in part) be hydrided also at room temperature when driven as a pressed powder electrode within the proper electrolytic environment. The activation consists of repeated charging-discharging cycles in aqueous K_2CO_3 where Fe surface oxides, attacked by carbonate anions, become suitable for cathodic reduction to metallic Fe. The activation rate is increased by using classical poisons of the hydrogen evolution reaction, such as thiourea or SeO_2.

When TiFe samples activated in carbonate were transferred to KOH (4–6 M), irreversible passivation occurred after cycling, which seemed to preclude this IMC from any electrochemical use. However, we subsequently found (Mengoli G, et al., unpublished results) that the cycle life of 50/50 TiFe is significantly improved when KOH is replaced by a 4 M KOH + 2 M LiOH mixture, as recommended for Ni-Fe and O_2-Fe alkaline batteries [3, 4].

All the data above point to one conclusion: that the presence of metallic Fe at the IMC surface and the actual reversibility of surface Fe redox reactions are the clue to both TiFe hydride formation and its cycle life in an electrochemical environment.

Therefore, the question remains: could electrode performance be improved with an alloy richer in Fe than the 50/50 compound? To address such a question we considered that Fe and Ti form two well-defined IMCs, stoichiometric TiFe and $TiFe_2$ [5] (AB and AB_2 families [6]). The latter does not absorb hydrogen but every composition richer in Ti than $TiFe_2$ does [7]. Thus, the present investigation concerns the commercially available 40/60 TiFe alloy.

Experimental

Materials

Two grades of 40/60 TiFe powder were used, both supplied by Goodfellow. One was already available by catalogue as the "alloy precursor", having particle size ≤ 150 μm and melting point

1380 °C (Goodfellow), which according to the producer is not a true alloy but is made by sintering a blend of powders of the component metals to achieve alloying by diffusion; the resultant cake is ground and sieved to the required particle size. The other "true alloy" was specially prepared at our request, again with particle size ≤ 150 μm and m.p. 1380 °C.

The 50/50 TiFe IMC was also supplied by Goodfellow. The Fe powder was of the following grades: "ferrum reductum" with particle size ≤ 50 μm supplied by Fluka and SNDC-NIFE material specially designed for Ni-Fe batteries.

The electrodes were prepared by inserting a weighed amount of powder(s) onto a weighed strip of Ni foam ("Sorapek") followed by pressing at 100–300 atm, fixing by immersion in a dilute solution of epoxy resin, and drying in hot air.

The chemicals for the electrolytic solutions, K_2CO_3, KOH, LiOH, thiourea and SeO_2, were all reagent grade. H_2O was of Millipore grade. N_2 was 99.9% purity gas from SIO.

Apparatus and procedure

TiFe powders were analyzed by X-ray diffraction with a Philips PV3710 instrument (Cu Kα radiation, 40 kV and 30 mA). The equipment included a silicon spinning holder and a graphite monochromator. The detected range was between 5° and 90° (2θ).

Scanning electron microscopy (SEM) observations were made by a Philips XL-40 LaB_6 apparatus. Quantitative standardless microanalyses were obtained using an energy dispersive analysis (EDAX) PV-99 X-ray spectrometer with a Be window.

The samples used as working electrodes in typical electrochemical tests were squares cut from the larger pressed powder strips prepared as above. Each square was pressure bonded to a Ni wire, which constituted support for the sample as well as the electrical connection. Table 1 gives the characteristics (composition, weight and dimensions) of the samples used for voltammetric and charging-discharging runs. The content of the active material for each sample was between 70% and 80% of the total weight.

The counter electrode was a Ni coil (diameter = 0.1 cm, $l = 50$ cm) rolled around the working electrode. The reference electrode was Hg|HgO-0.1 M KOH.

The three-electrode system was supported by the Teflon lid of a cylindrical uncompartmented Pyrex cell of 50 mL capacity. The cell was equipped with an inlet-outlet pipe system, which allowed a continuous N_2 draft to remove the gas produced by electrolysis. All experiments were carried out at 25 °C.

The electrochemical instrumentation consisted of AMEL and PAR apparatus interfaced with either an x-y recorder or a PC. Voltammetric and charging/discharging data were directly versus HgO. In the plots, the discharges are represented as working minus reference potential differences, ΔE, decreasing with time, thus mimicking the behaviour of a real battery.

The volumetric increments involved in the charging/discharging processes were monitored from the mechanical stress induced in specially designed asymmetrical electrodes. These consisted of pressed powder strips with contact to the electrolyte on only one face. The other face was masked with an insulating coating. One end of the strip was fixed to a support whereas the other was free to move in consequence to any volumetric changes. Although the

Table 1 Characteristics of the prepared TiFe samples

Sample	Active material (composition)	Net weight (g)	Dimensions (cm)
1	40/60 alloy	0.253	0.05×0.80×2.00
2	40/60 alloy	0.193	0.05×0.70×2.00
3	40/60 precursor	0.300	0.05×0.95×2.00
4	40/60 precursor	0.288	0.05×0.75×2.00
5	40/60 precursor	0.210	0.05×0.80×1.80
6	75% precursor + 25% Fe	0.230	0.05×0.90×2.00

described specimens likely have a porous structure, they do account for the volumetric changes occurring in the component particles; in fact, not only the powder particles are in tight contact since they were compacted under high pressure, but they are also bound to a non-rigid, light support (Ni foam) whereby the stress originated in the particles is transferred to the specimen, causing visible bending. Using a custom-made apparatus whose core is the arm of a balance directly applied onto the free end of the strip, any stress due to volumetric changes was directly measured by the weight (i.e., the force) necessary to offset it [8, 9].

Results and discussion

X-ray analysis

In order to set a standard for our X-ray analysis, the diffraction pattern of 50/50 TiFe IMC was first achieved by detecting three main lines at 43.104°, 62.49° and 78.77° (2θ), in full agreement with the provisions of the literature (JCPDS 19-636).

The "true" 40/60 TiFe alloy gave the diffraction pattern shown in Fig. 1. The lines marked by a cross can be ascribed to stoichiometric TiFe; those marked by a circle are likely due to $TiFe_2$ species, whereas those marked by a square might be explained by a hypothetical Ti_3Fe_5 phase; this last is suggested by comparison with the peaks present on the diffraction pattern of Ta_3Fe_5 (JCPDS 12-594). SEM observation coupled with EDAX analysis, however, showed a very homogenous particle composition at 40/60 TiFe atom ratio, pointing to a true alloy.

The X-ray pattern of the alloy precursor is shown in Fig. 2. The lines marked by a cross are very similar to those of pure Fe (JCPDS 6-966); the lines marked by a circle are similar to those of Ti (JCPDS 44-1294) except for a non-negligible shift with respect to the pure metal. Minor peaks marked by a square can again be ascribed to either 50/50 TiFe or to $TiFe_2$. Some of these lines are split due to the possible presence of hydrogen, the uptake of which might have occurred during the synthesis.
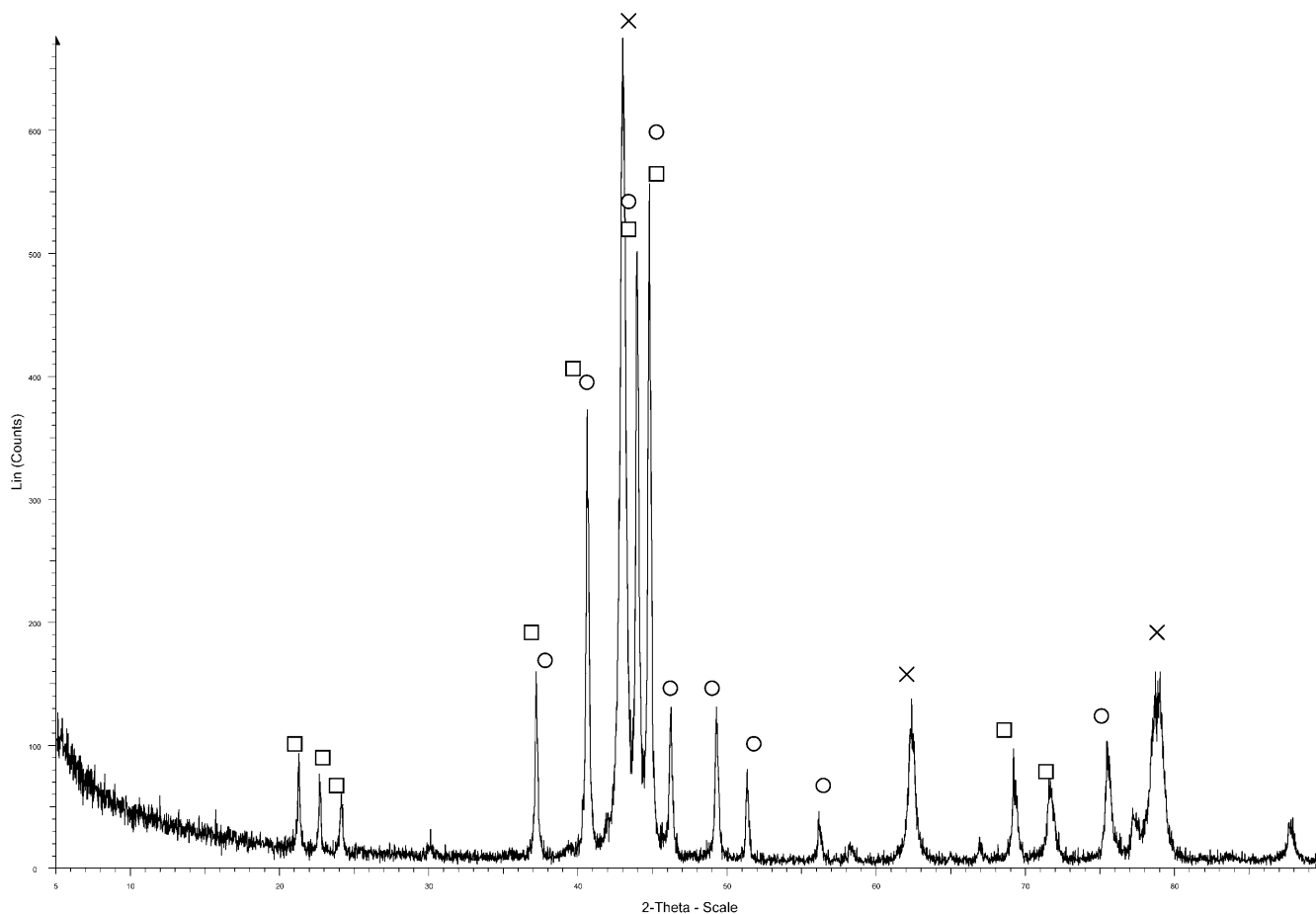
SEM observations coupled with EDAX analysis carried out in different spots and on different particles of this material have shown the presence of both Ti and Fe, but with a variable atom ratio which depended strongly upon either the sampled area or the sampled particle. In conclusion, X-ray and surface analysis point to a highly disordered system which more resembles a solid solution than an alloyed compound.

Electrochemical behaviour of 40/60 TiFe true alloy

The dotted curve of Fig. 3 shows the cyclic voltammogram (CV) ($v = 1$ mV s^{-1}) pattern achieved from sample 1 during one of the initial scans in 4 M KOH + 2 M LiOH. The currents were low and peak resolution was poor because of the high resistance of the surface layers. After 20 charging-discharging galvanostatic runs, carried out in aqueous K_2CO_3 with thiourea additive and then in KOH + LiOH (see below), the voltammetric

Fig. 1 Diffraction pattern of 40/60 TiFe true alloy. The lines are ascribed to 50/50 TiFe (*crosses*), $TiFe_2$ (*circles*), Ti_3Fe_5 (*squares*)

pattern evolved into that shown by the continuous curve: the charge engaged by CV ($v = 1$ mV s^{-1}) had increased, by now, many times. The cathodic branch formed a well-defined peak, followed by a shoulder jutting into the current, due to hydrogen evolution. On the reversal scan, in contrast, four peaks are outlined.

Based on our knowledge of the electrode behaviour of 50/50 TiFe IMC and of pure Fe [2], all the peaks in Fig. 3 can be ascribed to the redox reactions of surface Fe [10].

Hydrogen, absorbed by the TiFe alloy during polarization into the hydrogen evolution, is thus extracted at the first oxidation stage of Fe. However, at high loading and for fast scanning, hydrogen extraction cannot be exhaustive since it is controlled by diffusion within the alloy. During a voltammetric scan the electrode potential shifts to the successive surface Fe redox reactions, while hydrogen extraction continues overlapping them. This situation is illustrated by the broken curve of Fig. 3, which represents the linear sweep pattern ($v = 1$ mV s^{-1}) obtained after deep potentiostatic reduction (30 min at –1.350 V).

The redox systems of surface Fe were likewise seen to affect the shape of the galvanostatic discharges, as curves a and b in the insert of Fig. 3 demonstrate. In both cases the discharge occurred at two successive potential plateaus, but at a low discharge rate (curve a, $I = 2.5$ mA) most of the hydrogen was extracted before reaching the further potential of Fe oxidation.

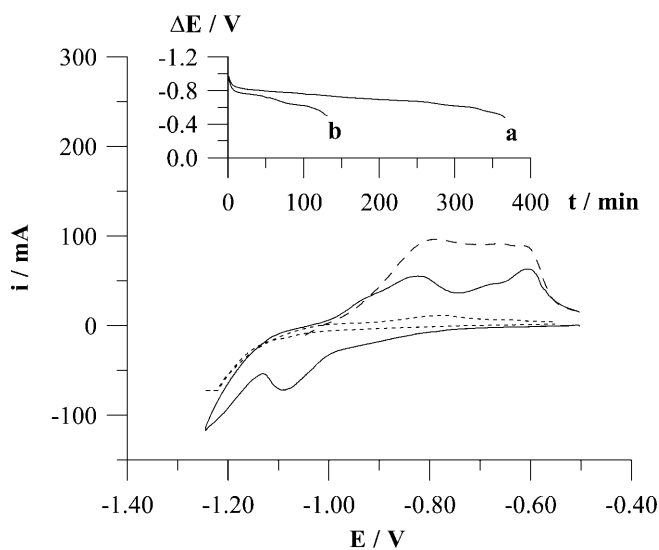The maximum charge stored in this sample was 62 mA h g^{-1}, ~25% of the theoretical hydrogen capacity of 40/60 TiFe alloy [7]. Figure 4 shows the evolution of the charge capacity with activation cycles of a latter true alloy electrode (sample 2). When not otherwise stated, the cycles were performed by charging with –300 mA×90 min, followed by discharging with 5 mA. During the initial 13 cycles, carried out in 4 M K_2CO_3, charge storage passed from ~11 to ~18 mA h g^{-1}. A charge increase was indisputably caused by two successive thiourea additions (final conc. 5×10^{-3} M), when at the 20th cycle ~80 mA h g^{-1} (~30% of theoretical capacity) was extracted after overnight (~14 h) charging. When sample 2 was transferred into 4 M KOH + 2 M LiOH, the charge capactiy has a loss (27th cycle), but rises again (29th cycle) after "poisoning" of the system with SeO_2. Prolonged charging overnight (~14 h) led again to recovery of more than 80 mA h g^{-1}. Afterward the charge storage fluctuated at lower levels.

The data of sample 2, while confirming those of sample 1, stress the reluctance of true alloy to become fully activated by hydrogen absorption.
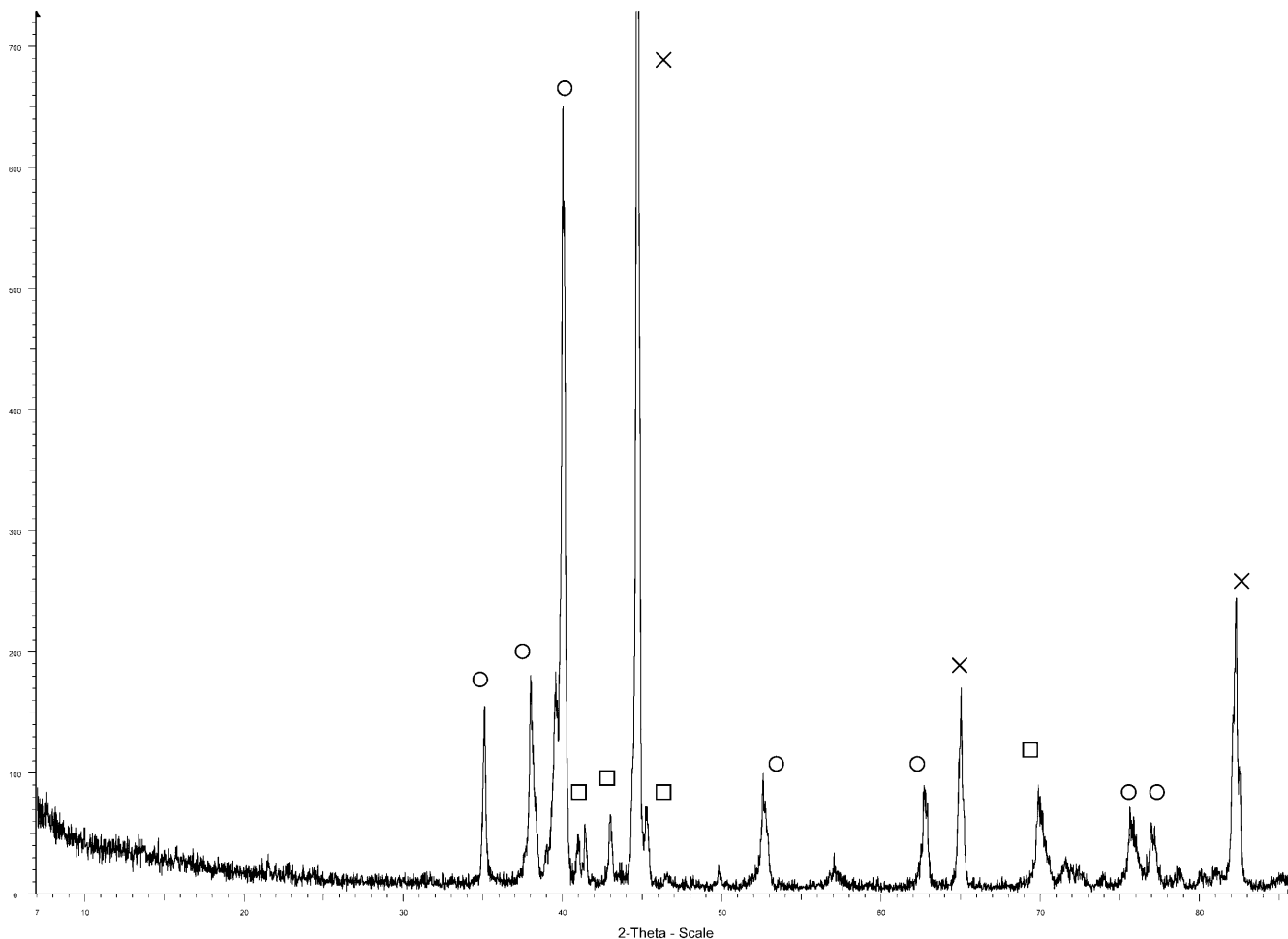
Fig. 2 Diffraction pattern of 40/60 TiFe alloy precursor. The lines are ascribed to Fe (*crosses*), Ti (*circles*), TiFe or TiFe$_2$ (*squares*)


Fig. 3 CV pattern ($v = 1$ mV s^{-1}) of 40/60 TiFe true alloy electrode (sample 1) in 4 M KOH + 2 M LiOH. *Dotted curve*: virgin sample; *plain curve*: activated sample; *broken curve*: LS voltammetry ($v = 1$ mV s^{-1}) recorded after potentiostatic reduction at –1.35 V. The *insert* represents the voltage versus time discharging plots of: (*a*) 2.5 mA ($j = 9.9$ mA g^{-1}) rate; (*b*) 5 mA ($j = 19.8$ mA g^{-1}) rate

Electrochemical behaviour of TiFe 40/60 alloy precursor

Activation in aqueous K$_2$CO$_3$

By following the activation procedure described above, the first 40/60 alloy precursor electrode (sample 3) was primarily investigated in aqueous K$_2$CO$_3$ by a series of charging-discharging cycles as reported in Table 2. The first cycle (not reported) consisted of a series of CV scans in 1 M K$_2$CO$_3$ within the potential range –0.20 to –1.30 V, after which the initially passivated sample began to develop a redox system. The charge recovered after galvanostatic reduction respectively at the 2nd and 3rd cycles, but remained low however, as shown in Table 2. Transfer into 4 M KOH initially led to more charge extraction (4th cycle) with a sharp decline in the subsequent cycles (5th to 7th). Cycling again in K$_2$CO$_3$ solution of different molarity (8th to 13th) had no significant effect: cycles 13–16 eventually accounted for the extent of self-discharge. No thiourea nor SeO$_2$ was employed here. The charge storage remained low and the activation in K$_2$CO$_3$ was clearly abandoned.
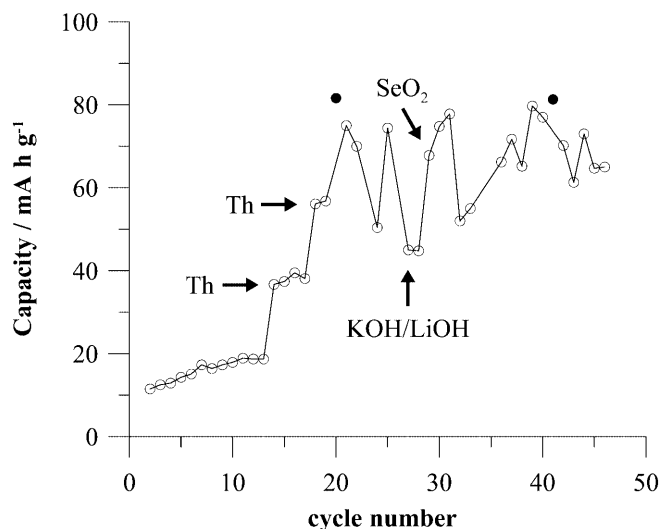
Fig. 4 Evolution of sample 2 charge storage with cycle number. The *arrows* indicate "poison" additives and/or electrolyte change. The *full points* represent discharges following overnight (~14 h) charging
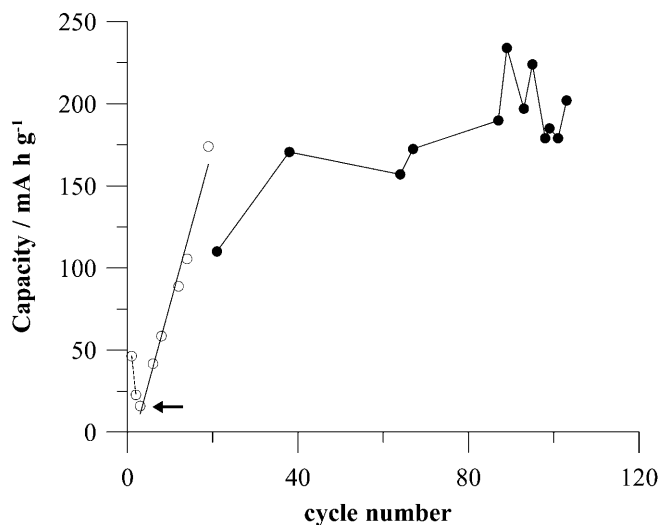
Fig. 5 Evolution of charge storage in 40/60 TiFe alloy precursor (sample 4) with cycle number. Discharging rates equal to: 5 mA (16.7 mA g^{-1}) (*open circles*); 20 mA (66.7 mA g^{-1}) (*filled circles*). The *arrow* indicates electrolyte change from 6 M KOH to 4 M KOH + 2 M LiOH

Table 2 Charge storage data of 40/60 TiFe alloy precursor (sample 3) in K_2CO_3 and KOH electrolytes

Cycle no.	Electrolyte	Charging conditions, I (mA)$\times t$ (h)	Delay (h)	Discharging, I (mA)	Storage (mA h g^{-1})
2	1 M K_2CO_3	−100×1.25	–	5	11.7
3	1 M K_2CO_3	−10×15	–	5	10.4
4	4 M KOH	−100×1.25	–	5	40.5
5	4 M KOH	−100×1.25	–	10	15.7
7	4 M KOH	−100×1.25	–	2.5	21.7
8	4 M K_2CO_3	−50×1.25	–	5	28.7
9	4 M K_2CO_3	−50×1.25	–	10	22.7
10	4 M K_2CO_3	−50×1.25	–	2.5	31.3
11	1 M K_2CO_3	−50×1.25	–	5	23.0
12	4 M K_2CO_3	−50×1.25	–	5	30.8
13	6 M K_2CO_3	−50×1.25	–	5	26.1
14	4 M K_2CO_3	−50×1.25	16	5	28.5
15	4 M K_2CO_3	−50×1.25	23	5	24.8
16	4 M K_2CO_3	−50×1.25	65	5	23.8

Activation in lithiated KOH

Charging-discharging runs of the second 40/60 alloy precursor electrode (sample 4) was initially carried out in 6 M KOH. Although, in the first run, nearly 50 mA h g^{-1} were extracted, the charge capacity declined immediately afterward. Consequently, the experiment was continued in 4 M KOH + 2 M LiOH. Figure 5 shows the evolution of the charge storage with cycle number. The cycles reported in Fig. 5 were performed by charging with ~250 mA×60 min followed by discharging either with 5 mA or, at a later stage, with 20 mA applied. Two points are duly noted. Firstly, the charge storage, in spite of some fluctuations, tended to increase throughout the entire cycle series.

The latter point concerns the low tolerance towards high discharging rates: while the charge extracted at the 20th cycle by 5 mA ($j = 16.6$ mA g^{-1}) was 175 mA h g^{-1}, the charge obtained at the subsequent cycle by 20 mA ($j = 66.6$ mA g^{-1}) was ~100 mA h g^{-1}. The maximum discharging rate sustained by the sample was in fact ~30 mA ($j \approx 100$ mA g^{-1}). Larger currents caused sharp drops in voltage with negligible charge extraction.

When measured at 20 mA, the charge capacity as shown in Fig. 5 settled at ~200 mA h g^{-1}, but was actually larger as the run in Fig. 6 demonstrates. Curve (a) represents a discharging plot with 20 mA applied, recorded immediately after charging with overall charge extraction of 235 mA h g^{-1}. Curve (b) represents a second discharge carried out by having simply left sample 4 at open circuit for 15 h after (a), which yielded another 56 mA h g^{-1}. Curve (c) shows the last discharge performed 40 h at open circuit after (b), with an eventual extraction of 21 mA h g^{-1}. An intrinsic charge capacity of ~300 mA h g^{-1} is consequently disclosed.

Coulombic efficiency of charging/discharging cycles

The fact that the sample after discharging still retained a significant amount of charge, and later becoming amenable to even further discharge, made the determination of charging/discharging efficiency rather problematic.
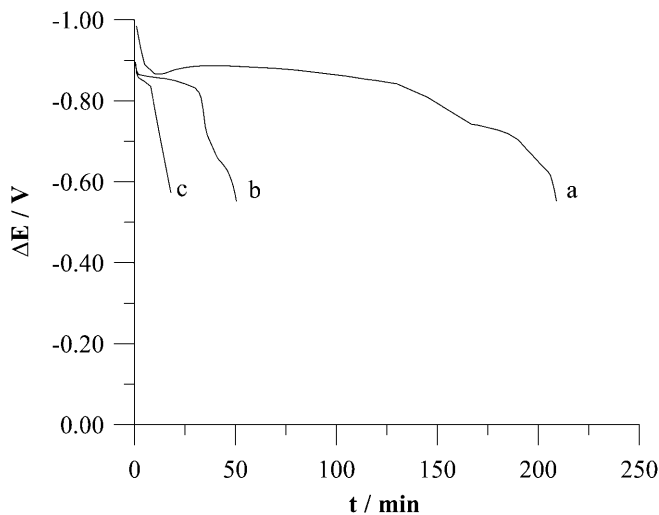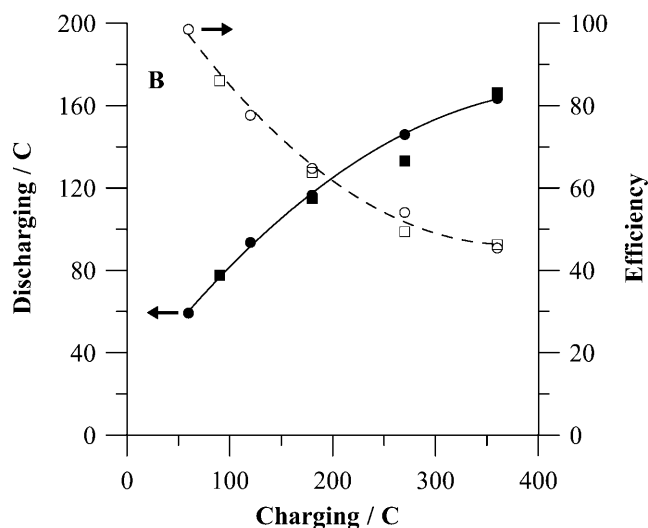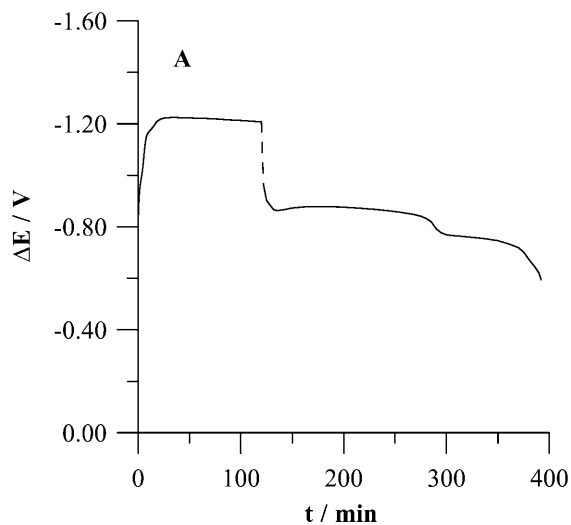
Fig. 6 Voltage versus time discharging plots representing: (*a*) the discharge immediately following the charge; (*b*, *c*) the extraction of the residual charge available in the sample after 15 h and 55 h, respectively, from (*a*) at open circuit. The rate of discharge was always $I = 20$ mA ($j = 66.7$ mA g^{-1})

For instance, when sample 4 was charged by –100 mA×30 min (180 C supplied), 130 C (72%) were then recovered at 10 mA rate, which thereupon changed to 106 (59%) when, prior to the cycle, the electrode had been discharged also of its "residual" charge. Therefore, the coulombic efficiency was here determined from the coulombic data averaged between two runs such as those just described. Charging currents were either –100 or –50 mA, while discharging was always by 10 mA. Figure 7a shows the voltage-time plot of a whole cycle (–50 mA/10 mA) typically utilized in the experiment. By using different charging times, the plots of Fig. 7b could eventually be constructed where the left ordinate, as a function of the charge supplied, gives the charge recovered while the right ordinate gives the coulombic yield. It can be deduced that the electrode, filled to 25% of its capacity, was charged/discharged at near 100% efficiency, which was still above 60%, to near 50% of capacity, to decline then for later storage. No coulometric yield difference appears in Fig. 7b from charging by –50 or –100 mA.

Self-discharge

Self-discharge was investigated by a series of runs in which the charge extracted immediately after charging was compared to that recovered when delaying the discharge by increasing the rest time at open circuit. During the rest time, a slight N_2 draft was made to bubble through the electrolyte to remove O_2 produced during electroysis and air contamination from outside. Charging was always made by –250 mA×60 min and discharging by $I = 10$ mA.

With exclusion of the initial time (~1 day), self-discharge was taking place at approximately the rate of 3%

Fig. 7 A Charging-discharging voltage versus time plot of sample 4 at –50/10 mA rate. **B** Coulombic efficiency of charging-discharging. The *abscissa* gives the charge supplied at (*circles*) –50 mA or at (*squares*) –100 mA rate. The *ordinate* on the *left* (*full symbols*) gives the charge correspondingly extracted at 10 mA rate, while the *ordinate* on the *right* (*empty symbols*) accounts for the coulombic yield

per day or below, so that after 3 weeks in open circuit the sample still retained ~45% of the initial storage. Such a rate is intrinsically fast for a practical battery, but if a major part of the charge had been stored as interstitial hydrogen, the rate appears very low. In fact, not only is a decomposition pressure of some atmospheres expected [7] for 40/60 TiFe hydride, but hydrogen loss occurred here in a vented system when the H_2 equilibrium pressure could never be established.

Poison (SeO_2) effect on charge storage

To confirm previous data on the charge storage of the 40/60 alloy precursor, a new electrode (sample 5) was

employed. Figure 8 shows the evolution of charge capacity with cycle number. Charge was made also by –250 mA×60 min, followed by discharging with either 5 mA ($j \approx 24$ mA g^{-1}) or 10 mA ($j \approx 48$ mA g^{-1}). During the initial nine cycles performed in 6 M KOH, the capacity remained between 15–20 mA h g^{-1}. Beginning with the 10th cycle, the sample was transferred into 4 M KOH + 2 M LiOH. In this latter electrolyte the charge storage increased steadily for tens of cycles until it attained a rather constant level of $\sim$130 mA h g^{-1}, well below the capacity of sample 4. At the 61st cycle, the electrolyte was made to 5×10^{-3} M in SeO$_2$ and the charge storage nearly doubled. The insert in Fig. 8 shows the discharging plots recorded before and after poisoning with SeO$_2$. The charge capacity thus achieved was maintained in subsequent cycles; sample 5 also manifests a low tolerance for a high discharging current.

Dilatometric test

The insertion of interstitial hydrogen into a metal lattice is generally accomplished with volume expansion; the redox reactions of the metal are also accomplished with dimensional stress when the metal surface is, for instance, oxidized to an insoluble oxide layer having a different density from the parent metal.

Since direction and size of the stress due to hydrogen are unlikely to match those involved in a redox metal system, a dilatometric test can diagnose the charge storage process actually occurring.
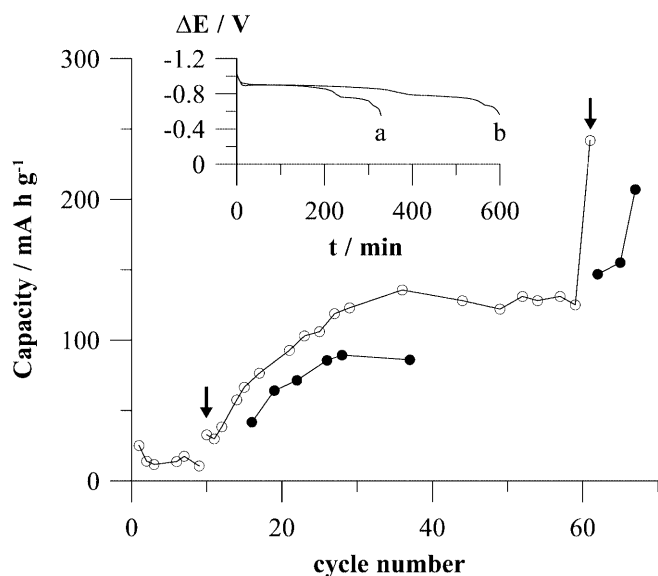
Fig. 8 Evolution of sample 5 charge storage with cycle number. Discharging rates equal to: 5 mA (23.8 mA g^{-1}) (*open circles*); 20 mA (95.2 mA g^{-1}) (*filled circles*). The *first arrow* indicates electrolyte change from 6 M KOH to 4 M KOH + 2 M LiOH. The *second arrow* indicates SeO$_2$ addition. The *insert* accounts for the discharging plots achieved (*a*) before and (*b*) after SeO$_2$ addition. The discharging rate was $I = 5$ mA

Table 3 gives the characteristics of the asymmetrical strip electrodes used for comparing the stress of pure Fe with that of TiFe. The Fe used for the test was of SNDC-NIFE grade, while 40/06 TiFe was of alloy precursor grade.

Prior to the dilatometric experiment, both the samples underwent several activation cycles in 4 M KOH + 2 M LiOH containing thiourea (2×10^{-3} M) in order to speed up the activation process. It must, however, be noted that full activation could not be achieved, since the electrodes contacted the electrolyte on only one face (see Experimental).

Test results are illustrated in Figs. 9, 10, 11. The ordinate of the upper part of each figure (A) accounts for the force (see Experimental) originated by the volumetric stress as a function of both the sample charge (reported on the abscissa) and the direction of the process (charging or discharging, indicated by the arrows). The ordinate on the lower part of the figure (B) gives the voltage as a function of previous variables.

Upon reviewing the discharging plots for Fe, we see (Fig. 9a, plain curve) that, after slight oscillations, a volumetric stress definitely occurred in coincidence with the conversion of metallic Fe into the less dense Fe^{II} species. The occurrence of this reaction is otherwise indicated by the first plateau of the voltage plot (Fig. 9b, plain curve). The subsequent Fe$^{II} \rightarrow$ Fe^{III} conversion took place with stress relaxation due to the higher density of the Fe^{III} species with respect to those of Fe^{II} (Fig. 9a). The voltage plot correspondingly outlines a later plateau for Fe^{II} oxidation (Fig. 9b).

During the charging process (broken curves, beginning at the right side of Fig. 9), both the force and voltage behaviour seen above are reversed, although with large hysteresis with respect to the discharge.

Upon considering the discharging process of 40/60 TiFe precursor (plain curves of Fig. 10), we observe (Fig. 10a) that relaxation of the volumetric stress took place immediately and continued to $\sim$20% of full discharge. The phenomenon was clearly related to TiFe shrinking due to hydrogen extraction. The subsequent stress increase is accounted for by the Fe$\rightarrow$Fe^{II} reaction, whereas the final stress relaxation can again be explained by the Fe$^{II} \rightarrow$ Fe^{III} process. However, the voltage plot (Fig. 10b, plain curve), which outlines a much smoother transition among the three main discharge plateaus than in Fig. 9b (the voltage of the Fe$^{II} \rightarrow$ Fe^{III} transition in Fig. 9b is fitted only by the third plateau of Fig. 10b), suggests that hydrogen extraction was occurring, although coupled with Fe oxidation, along the entire discharge.

Table 3 Characteristics of the asymmetrical strip electrodes used for the dilatometric test
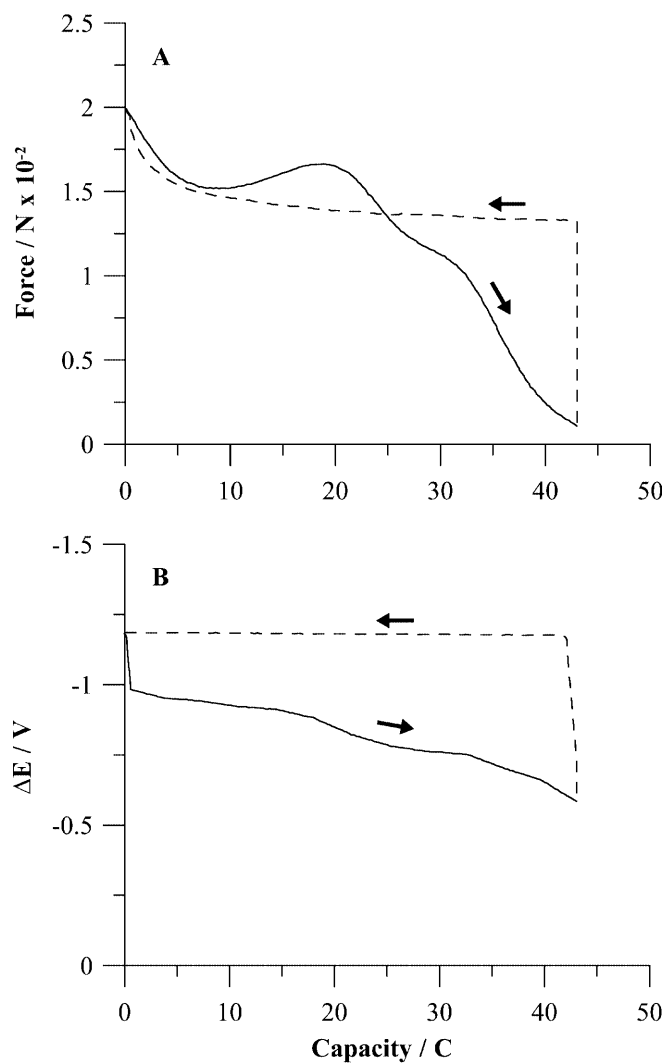
Active material	Net weight (g)	Dimensions (cm)
Fe (NIFE)	0.080	0.07×0.50×2.40
40/60 TiFe alloy precursor	0.120	0.07×0.50×2.80
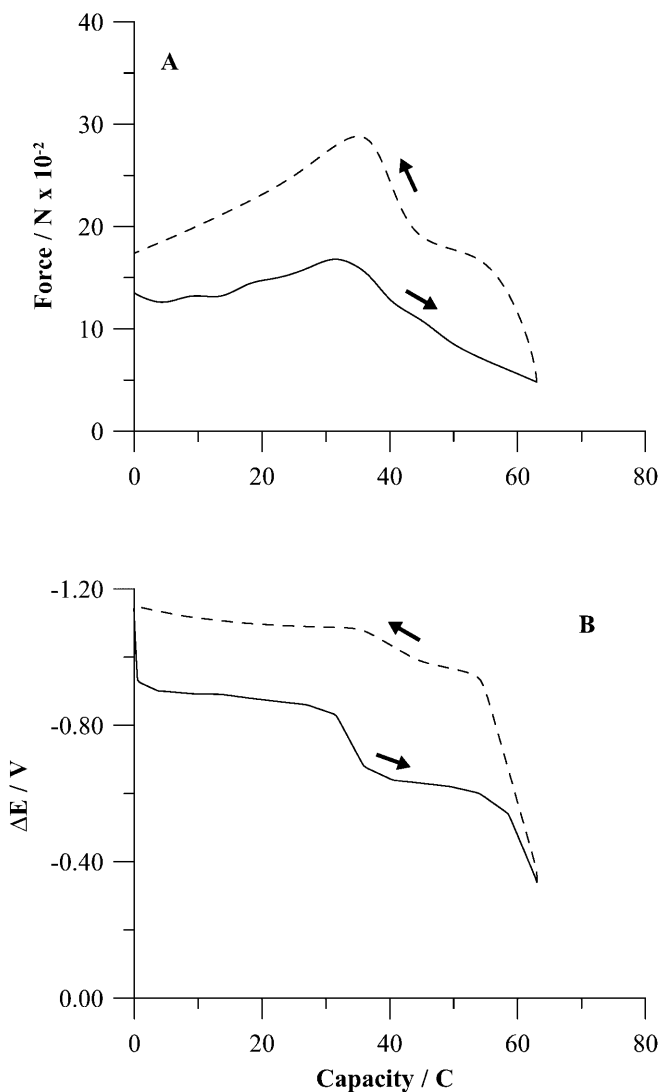
Fig. 9 A Dilatometric plot of a Fe pressed powder electrode during a charge (*broken curve*)-discharge (*plain curve*) cycle as a function of the charge stored in the sample. **B** Charging (*broken curve*)-discharging (*plain curve*) ΔE versus charge plot of the Fe electrode. Charging rate 10.2 mA; discharging rate 5 mA

Fig. 10 A Dilatometric plot of a 40/60 TiFe alloy precursor sample electrode. **B** Charging-discharging plot of the 40/60 sample. The conditions are the same as in Fig. 9 except for the currents which were –12 mA for charging and 4 mA for discharging

This view is strengthened by the features of the charging process (Fig. 10, broken curves). A sharp, steadily increasing stress is indicated by the dilatometric plot (Fig. 10a) while the voltage rose sharply without outlining any $Fe^{III} \rightarrow Fe^{II}$ reduction. It is consequently likely that the "discharged" TiFe sample still contained a significant amount of hydrogen which, by diffusing from the bulk, contributed to Fe surface reduction with rapid restoration of the electrode potential.

In a later test on a TiFe sample, the charging and discharging processes were both pushed to a depth greater than in Fig. 10. Therefore, during the discharge (Fig. 11a, plain curve), one observes that the relaxation due to volume contraction spanned a force range much wider than in Fig. 10a, which probably implies the engagement 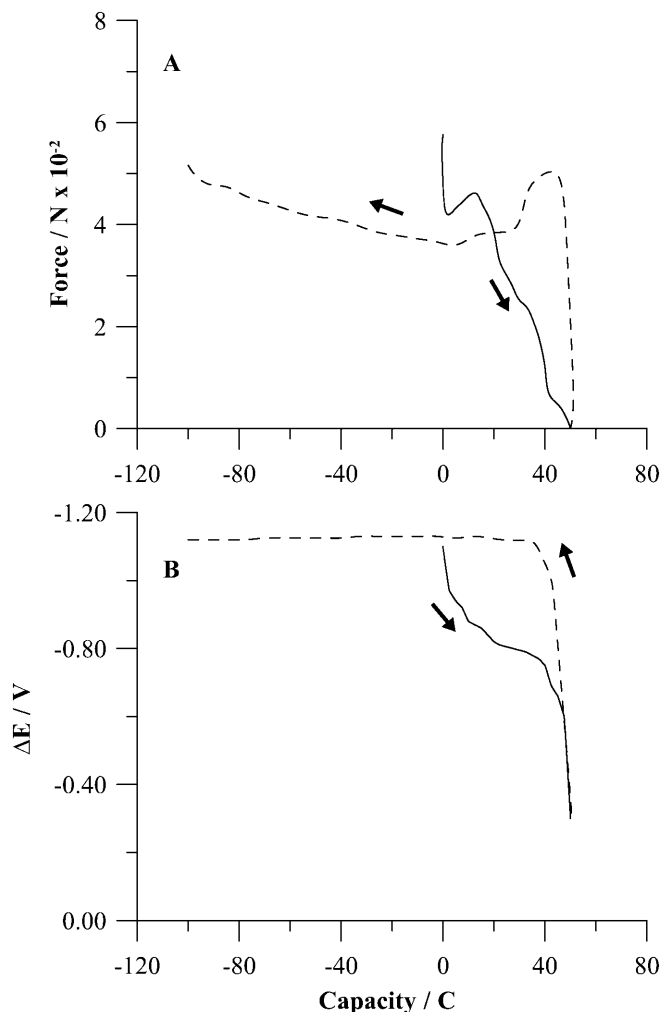of more hydrogen (discerned from the plot shape) and eventually more Fe than before. Thus 20% more charge was indeed extracted but the discharge pushed to –0.25 V (Fig. 11b) was causing passivation, which then decreased the coulombic efficiency of subsequent charging. New information could however be obtained from the corresponding dilatometric test (Fig. 11a, broken curve). The occurrence of both $Fe^{III} \rightarrow Fe^{II}$ and $Fe^{II} \rightarrow Fe^{III}$ (absent in Fig. 10a) is now evident, followed by the volumetric increase slowly induced by hydrogen insertion.

Electrochemical behaviour of the (TiFe precursor + Fe) composite

This electrode (sample 6) was prepared by the simple mechanical mixture of 40/60 TiFe alloy precursor with Ferrum reductum by a 3:1 weight ratio. It was activated
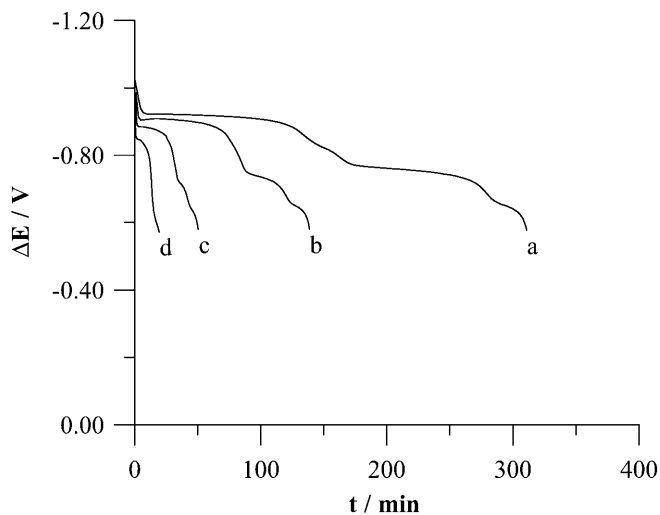
Fig. 11 A Dilatometric plots of the sample of Fig. 10 carried out under deeper charging-discharging conditions. **B** The corresponding voltage versus charge plots

Fig. 12 Voltage versus time discharging plots of (TiFe + Fe) composite electrode (sample 6). Discharging rates were: (*a*) 10 mA (*j* = 43.5 mA g^{-1}); (*b*) 20 mA (*j* = 87 mA g^{-1}); (*c*) 40 mA (*j* = 174 mA g^{-1}); (*d*) 80 mA (*j* = 348 mA g^{-1})

Direct engagement of the added Fe into the charging-discharging cycles is indeed evidenced by the shape change of the plots of Fig. 12 with respect to the analogues of 40/60 TiFe pure alloy and/or precursor. The transition between the discharging plateaus is much sharper here and strongly resembles the behaviour of the pure Fe electrode of Fig. 9b; a greater tolerance to relatively high discharging rates is also apparent in Fig. 12.

Conclusion

The two TiFe grades studied in this work have shown a substantially different ability to store charge, which can be explained by their profound structural differences.

Yet as a true alloy, the 40/60 atom ratio does not fit a real stoichiometry but primarily, as shown by X-ray analysis, a mixture of stoichiometric TiFe and TiFe$_2$. Since the latter does not form any hydride phase, all the ability to absorb hydrogen stems from the 50/50 TiFe fraction present in the alloy. Accordingly, in the pioneering work on formation and properties of iron-titanium hydrides [7], an intake of 50% less hydrogen than in the stoichiometric TiFe was found for the 40/60 composition.

Only 30% of the said hydride (TiFeH) was here achieved from the electrolytic environment, probably due to the difficulty for discharged hydrogen to reduce and permeate the very regular 40/60 surface texture evidenced by EDAX analysis.

What can we conclude about the 40/60 TiFe alloy precursor? After repeated cycling in lithiated KOH, the 40/60 TiFe alloy precursor has shown a remarkable ability to store charge. The redox processes of surface Fe contribute significantly to the charge capacity but absorbed hydrogen most probably plays a fundamental role, as indicated by the following:

directly in 4 M KOH + 2 M LiOH by continuous CVs at *v* = 5 mV s^{-1} within the potential range –0.55 to –1.30 V.

The CV scans prolonged over 24 h increased the charge capacity to a rather constant value of ∼100 mA h g^{-1}, whereby further activation was induced by a series of galvanostatic charging-discharging cycles carried out as previously described. The typical ΔE versus time discharging plots achieved after 20–25 activation cycles are shown in Fig. 12. The charge thus extracted, for instance at the 10 mA rate, was 255 mA h g^{-1}, which, by summing up 91 mA h g^{-1} of residual charge extracted later on, leads the intrinsic capacity to above 300 mA h g^{-1}, which is not too different from that of pure 40/60 alloy precursor samples.

The theoretical capacity of the Fe→Fe^{II} reaction is above 900 mA h g^{-1} (the practical capacity is 2/3 lower), but for the Fe grade used in sample 6 the actual capacity was ∼100 mA h g^{-1} after 50 activation cycles (Mengoli G, et al., unpublished results). Therefore, the capacity achieved here from the composite electrode is not surprising.

1. The dilatometric test, whereby the volumetric (i.e., stress) changes that take place during charge driving at the 40/60 TiFe alloy precursor electrode appear to be closer to those expected for a hydrogen absorber than for those of pure Fe.

2. The large effect of "poisons". It is recalled that charge storage nearly doubled (see Results and discussion, Fig. 10) within a single cycle after the addition of SeO_2, a typical promoter of hydrogen absorption.

3. The high reluctance of the material to fast-charge draining, which points to the diffusional constraint typical of interstitial hydrogen. Figure 12 instead shows significant changes in the discharging patterns of the TiFe alloy precursor caused by a minor amount of Fe.

The question therefore is to establish how and where hydrogen is entering and then storing itself in the alloy precursor. As far as the permeation is concerned, EDAX analysis has revealed a large composition discontinuity so that surface areas are much richer in Fe than would be expected for a 40/60 composition. The surface areas are more easily reduced to metallic Fe, which then catalyzes the dissociative hydrogen permeation within the material.

With regard to the species upon which hydrogen locates, 50/50 TiFe most likely plays a minor role since X-ray analysis has shown weak diffraction in this structure. In contrast, the diffraction pattern of the 40/60 alloy precursor, primarily accounted for by its similarity to Fe and Ti lines, points to Ti as the main hydrogen absorber, acting as Ti hydride. Not only is the amount of hydrogen stored in TiH_2 about twice the storage of 50/50 TiFe, but Ti embedded within a Fe-rich matrix obviates the passivity of the metal towards hydrogen absorption, typical of alkaline media. Hydrogen storage on Ti explains the low self-discharge rate from the vented system tested above (see Results and discussion), since the decomposition pressure of TiH_2 is some order of magnitude lower than that of TiFe analogues.

A short comment is finally made on the application perspective, if any, of the investigated material which, inter alia, probably is the cheapest among the IMCs. With respect to a Fe anode to which the 40/60 TiFe precursor has likely to be compared, lower capacity and much lower ability to sustain high discharging rates have at present be evidenced. However, these drawbacks could, in part, be obviated with the use of more finely ground, or even nanostructured, powders. Furthermore, the fact that a large amount of charge is stored on hydrogen could make the 40/60 alloy precursor, different from Fe, suitable for use in sealed batteries with all the advantages inherent in a closed battery system.

References

1. Schlapbach L (1992) Surface properties and activation. In: Schlapbach L (ed) Hydrogen in intermetallic compounds II, Topics in Applied Physics, vol 67. Springer, Berlin, pp 76–79
2. Bernardini M, Comisso N, Davolio G, Mengoli G (2000) J Electroanal Chem 487:1
3. Falk SU, Salkind AJ (1969) Alkaline storage batteries. Wiley, New York, pp 613–619
4. McBreen J (1981) Secondary batteries – introduction. In: Bockris JO'M, Conway BE, Yeager E, White RE (eds) Comprehensive treatise of electrochemistry, vol 3. Plenum, New York, p 326
5. Elliot RP (1965) Constitution of binary alloys, first supplement. McGraw-Hill, New York
6. Kleperis J, Wjcik G, Czerwinski A, Skowronski J, Kopczyk M, Beltowska-Brzezinska M (2001) J Solid State Electrochem 5:229
7. Reilly JJ, Wiswall RH Jr (1974) Inorg Chem 13:218
8. Davolio G, Soragni E, Fontanesi C (1996) The Electrochemical Society meeting abstracts, vol 96-101. The Electrochemical Society, Pennington, NJ, abstr 69
9. Davolio G, Soragni E (1998) J Appl Electrochem 28:1313
10. Burke LD, Lyons MEG (1986) Electrochemistry of hydrous oxide films. In: White RE, Bockris JO'M, Conway BE (eds) Modern aspects of electrochemistry, vol. 18. Plenum Press, New York, p 169